

Cite this: *J. Mater. Chem. A*, 2018, 6, 24194

# Paragenesis BN/CNTs hybrid as a monoclinic sulfur host for high rate and ultra-long life lithium–sulfur battery†

Bin He,<sup>a</sup> Wen-Cui Li,<sup>a</sup> Yu Zhang,<sup>a</sup> Xiao-Fei Yu,<sup>a</sup> Bingsen Zhang,<sup>b</sup> Feng Li<sup>b</sup> and An-Hui Lu<sup>\*,a</sup>

For lithium–sulfur (Li–S) batteries, it is critical to design advanced host materials with high conductivity and strong binding interactions with sulfur species to trap and convert the polysulfides efficiently. Here, we report a novel BN/CNTs hybrid with paragenesis structure, high surface area and O-doping *via* a one-step co-pyrolysis method. Such paragenesis structure can remarkably lower the contact resistance between non-conducting BN and conductive CNTs, and the O dopant in BN can narrow the bandgap of BN, both imparting the BN/CNTs hybrid a high conductivity of 1884 S m<sup>-1</sup>. The BN/CNTs hybrid hosted sulfur shows monoclinic phase instead of the generally reported orthorhombic phase, implying a strong interaction between sulfur and the BN/CNTs hybrid. Moreover, the high surface and the O doping enable BN/CNTs hybrid to adsorb polysulfides with a superior capacity due to the polarization of electrons away from the sulfur atoms towards BN/CNTs. Thus, the BN/CNTs–sulfur cathode can deliver high specific capacity (1374 and 1068 mA h g<sup>-1</sup> at 0.2C and 1C, respectively), superior cycling stability (a constant coulombic efficiency of ~99% and a decay rate of 0.045% per cycle along with 500 cycles at 1C) and excellent rate capability (840 mA h g<sup>-1</sup> at 4C). Moreover, it exhibits good high-sulfur-loading areal capacity (up to 4.5 mA h cm<sup>-2</sup>) with stable cell performance.

Received 3rd October 2018  
Accepted 27th October 2018

DOI: 10.1039/c8ta09564g

rsc.li/materials-a

## Introduction

Lithium–sulfur (Li–S) battery with a high energy density (2600 W h kg<sup>-1</sup>) is expected to replace the conventional lithium-ion battery for applications in electric vehicles and unmanned planes.<sup>1–3</sup> The low utilization of sulfur and rapid capacity fading of sulfur cathode limit the commercialization of the current Li–S battery.<sup>4–6</sup> Confining sulfur within carbon materials is an effective way to improve the conductivity of insulated sulfur and trap the highly soluble lithium polysulfides (LiPSs) generated during the discharge–charge process.<sup>7–9</sup> Many research teams have made strides in the design of suitable advanced porous carbons.<sup>10–14</sup> Nevertheless, the interactions between nonpolar carbon and polar LiPSs are too weak to efficiently restrain LiPSs dissipation during the long charging cycles.<sup>15–19</sup>

Polar materials are known to be capable of forming relatively strong chemical bonds with LiPSs, thus effectively trapping LiPSs species.<sup>20,21</sup> Polar metal oxides (*e.g.* TiO<sub>2</sub>,<sup>22</sup> CeO<sub>2</sub>,<sup>23</sup> and MnO<sub>2</sub> (ref. 24)) and metal sulfides (*e.g.* NiS<sub>2</sub>,<sup>25</sup> Co<sub>9</sub>S<sub>8</sub> (ref. 26) and

FeS<sub>2</sub> (ref. 27)) as well as metal nitrides (*e.g.* TiN<sup>28</sup> and Co<sub>4</sub>N<sup>29</sup>) have been developed as additives or as direct sulfur hosts to improve the cycling stabilities of sulfur cathodes. Unfortunately, the inherently low specific surface areas of these polar metallic compounds (<100 m<sup>2</sup> g<sup>-1</sup>; see Table S1, ESI†) make them unsuitable for trapping large amount of LiPSs based on monolayer chemical adsorption. As a consequence, LiPSs molecules further away from the surface can dissolve into the electrolyte and shuttle between the electrodes. Thus, an appropriate sulfur host should possess both strong LiPSs affinity and high specific surface area for trapping large amount of LiPSs.

Furthermore, most polar metallic compounds exhibit low electrical conductivity, which could hinder electron transport and induce slug interfacial redox reaction kinetics,<sup>16</sup> leading to further decreased sulfur utilization. Although conductivities of these polar materials can be improved by physical mixing or blending with carbon materials, abundant interfaces between the polar metallic compounds and the carbon materials will be generated, thus causing substantial contact resistance. During cycling, such high contact resistance in an electrode leads to increased Joule heating, which worsens cycle stability and reduces safety of sulfur electrodes.<sup>30</sup> Moreover, the high contact resistance leads to unsatisfactory conductivity. For instance, though hollow TiO<sub>2</sub> physically webbed with carbon nanotubes is employed as a sulfur host for Li–S cathode, the conductivity of

<sup>a</sup>State Key Laboratory of Fine Chemicals, School of Chemical Engineering, Dalian University of Technology, Dalian 116024, P. R. China. E-mail: anhuilu@dlut.edu.cn

<sup>b</sup>Shenyang National Laboratory for Materials Science, Institute of Metal Research, Chinese Academy of Sciences, Shenyang 110016, China

† Electronic supplementary information (ESI) available. See DOI: 10.1039/c8ta09564g

such TiO<sub>2</sub>/carbon nanotubes composite is only 14 S m<sup>-1</sup>.<sup>31</sup> Obviously, an effective approach for the preparation of sulfur host materials with high electrical conductivity and strong LiPSs affinity is urgently needed.

Herein, we report a highly conductive BN/CNTs hybrid with paragenesis structure, high surface area and O-doping *via* a one-step co-pyrolysis method. Such hybrid material exhibits an exceptionally high conductivity of 1884 S m<sup>-1</sup>, with strong LiPSs binding property. When used as a sulfur host, the obtained BN/CNTs-sulfur cathode can achieve excellent cycling ability over 500 cycles and outstanding rate capability up to 840 mA h g<sup>-1</sup> at 4C. Specifically, the cathode with a high areal sulfur loading of 4.25 mg cm<sup>-2</sup> exhibits a reversible areal capacity of about 4.5 mA h cm<sup>-2</sup>.

## Experimental

### Chemicals

All chemicals were used as received without any further purification. Urea (99.0%), cobalt(II) acetate tetrahydrate (99.5%) and boric acid (99.5%) were purchased from Sinopharm Chemical Reagent Co. Ltd. Deionized water was used for all experiments.

### Fabrication of p-BN/CNTs-S composite

Typically, suitable amounts of urea, boric acid and cobalt(II) acetate tetrahydrate with molar ratio of 240 : 20 : 1 were homogeneously mixed and heated in a tube furnace at 900 °C in Ar gas for 2 hours. After cooling down naturally, the obtained black powder was soaked in 8 M HCl aqueous solution for 24 h to partially remove the Co catalyst. Subsequently, the prepared sample was intensively washed with hot water for 8 h. The resulting BN/CNTs hybrid, named as p-BN/CNTs, was filtered, washed with distilled water, and dried at 80 °C. The prepared p-BN/CNTs (0.0996 g) and sulfur (0.2182 g) were ground together, heated to 155 °C in a sealed quartz bottle for 12 h and then heated at 400 °C for 1 h. p-BN/CNTs-S composite (0.2857 g) was obtained. Thus, the theoretical sulfur content in p-BN/CNTs-S was 65.1 wt%, which is almost equal to the TGA result. p-BN/CNTs-S with sulfur content of 75 wt% was also prepared with the same procedure and appropriately increased sulfur amount.

### Synthesis of control sample

Typically, the suitable amount of urea and boric acid were homogeneously mixed at a molar ratio of 12 : 1 and then heated in a tube furnace at 900 °C in Ar gas for 2 hours. After cooling down naturally, the obtained white powder was soaked in 8 M HCl aqueous solution for 24 h. Subsequently, the prepared sample was intensively washed with hot water for 8 h. The resulting BN, designated as O-BN, was filtered, washed with distilled water, and dried at 80 °C. O-CNTs powders were prepared by oxidization of CNTs with HNO<sub>3</sub>. In a typical procedure, 0.1 g of raw multiwalled CNTs were suspended in 50 ml of concentrated nitric acid and refluxed at 120 °C in an oil bath for 2 h. After the mixture was cooled down to room temperature, it was filtered and washed with deionized water. Then, the product was dried at 60 °C for 12 h and denoted as O-

CNTs. For preparation of O-CNTs and O-BN composites, O-CNTs powder and the prepared O-BN were first mechanically mixed for 1 h, at a mass ratio of 7 : 3. The obtained mixture was named as BN/CNTs-M. Next, BN/CNTs-M (0.1003 g) and sulfur (0.2246 g) were ground together, heated to 155 °C in a sealed quartz bottle for 12 h and then heated to 400 °C for 1 h. Carbon-sulfur hybrid BN/CNTs-M-S (0.2885 g) was obtained. Thus, the theoretical sulfur content in BN/CNTs-M-S was 65.2 wt%. O-CNTs-S was prepared by heating a mixture of O-CNTs powder and sulfur using the above-mentioned method, to achieve a sulfur content of 65.2 wt%.

### Preparation of Li<sub>2</sub>S<sub>6</sub>

A 10 mM Li<sub>2</sub>S<sub>6</sub> solution was prepared by dissolving elemental S and Li<sub>2</sub>S at a molar ratio of 5 : 1 in a binary solution of DOL and DME. The solution was stirred at 50 °C for 72 h.

### Li<sub>2</sub>S<sub>6</sub> adsorption study and XPS sample preparation

To quantitatively evaluate the adsorptivity of p-BN/CNTs, O-BN and O-CNTs toward Li<sub>2</sub>S<sub>6</sub>, UV/Vis absorption spectroscopy was used to measure the solution concentration of Li<sub>2</sub>S<sub>6</sub> after adsorption. Three samples of the respective adsorbents with the same mass (30 mg) were individually mixed with 3 ml of 10 mM Li<sub>2</sub>S<sub>6</sub> solutions in DME/DOL (50 : 50 v/v). After standing for 24 h, 0.4 ml of the obtained solution was diluted into 2.0 ml of DME/DOL (50 : 50 v/v) for UV/Vis spectroscopy. O-BN, p-BN/CNTs and O-CNTs were individually mixed with 10 mM Li<sub>2</sub>S<sub>6</sub> in an Ar-filled glovebox to obtain O-BN-Li<sub>2</sub>S<sub>6</sub>, p-BN/CNTs-Li<sub>2</sub>S<sub>6</sub> and O-CNTs-Li<sub>2</sub>S<sub>6</sub> solutions, respectively. The obtained mixtures were then settled for 12 h to visually inspect the color changes. Afterwards, the suspensions were centrifuged and the solids were obtained for XPS analysis after drying under vacuum for 24 h. All procedures were performed in an argon-filled glovebox.

### Characterization

Morphologies of the samples were investigated by field-emission scanning electron microscopy (SEM) using a Hitachi S-4800 instrument at 10 kV. Nitrogen adsorption isotherm was measured at 77 K with an ASAP 3000 adsorption analyzer (Micromeritics). Before these measurements, all samples were degassed at 200 °C for 6 h until the pressure was below 5 Pa. The Brunauer-Emmett-Teller (BET) method was used to calculate the specific surface areas ( $S_{\text{BET}}$ ). Total pore volumes were calculated from the amount adsorbed at a relative pressure  $P/P_0$  of 0.99. X-ray diffraction (XRD) patterns were obtained with a Rigaku D/MAX-2400 diffractometer using CuK $\alpha$  radiation (40 kV, 100 mA,  $\lambda = 1.54056 \text{ \AA}$ ). Transmission electron microscopy (TEM) analyses were carried out with a FEI Tecnai G2 F20 microscope equipped with GIF and high angle annular dark field (HAADF) detector operating at 200 kV. Samples for TEM analyses were prepared by dropping a drop of ethanol solution of the products on carbon-coated copper grids and drying at room temperature. Thermogravimetric analysis (TGA) of p-BN/CNTs was measured from 40 to 800 °C with a heating rate of 10 °C min<sup>-1</sup> under an air flow, while TGA of p-BN/CNTs-sulfur

was measured from 40 to 600 °C with a heating rate of 10 °C min<sup>-1</sup> under a nitrogen flow, both using a STA449 F3 Jupiter thermogravimetric analyzer (NETZSCH). The adsorption performance of lithium polysulfide was measured using a UV-Vis spectrophotometer. Fourier transform infrared (FTIR) spectra were collected using a Thermo Scientific Nicolet 6700 spectrometer by dispersing samples in KBr pellets. X-ray photoelectron spectroscopy (XPS) data were obtained with a PHI 5000 Versaprobe spectrometer equipped with an Al K $\alpha$  X-ray source. Conductivity of p-BN/CNTs was tested by a four-tip probes method.

### Electrochemical measurements

Electrochemical experiments were performed using CR2025 coin-type test cells assembled in an argon-filled glovebox with lithium metal as the counter and reference electrodes. The cathode of the lithium-sulfur batteries was prepared by mixing 75 wt% of the hybrid material, 15 wt% conductive additives (CNTs) and 10 wt% polyvinylidene difluoride (PVDF) in *N*-methyl-2-pyrrolidone (NMP) to form a slurry that was pasted onto a carbon-coated aluminum foil. A Celgard 2400 membrane was used as the separator. The electrolyte was 1 M LiTFSI in DME : DOL (1 : 1, v/v) containing 3 wt% LiNO<sub>3</sub>. Discharge/charge measurements were conducted at a voltage interval of 1.7 to 2.8 V using a Land CT2001A battery test system. Cyclic voltammetry (CV) measurements were performed on a CHI660D electrochemical workstation at a scan rate of 0.1 mV s<sup>-1</sup>. Electrochemical impedance spectroscopy (EIS) measurements were carried out before charge-discharge cycles in the frequency range 100 kHz to 0.01 Hz on the CHI660D.

## Results and discussion

The BN/CNTs hybrid was prepared using a mixture of boric acid, urea and cobalt acetate precursors *via* a one-step co-pyrolysis method, which facilitates growth of the paragenesis structure formed between boron nitride (BN) and carbon nanotubes (CNTs). In the synthesis process, H<sub>3</sub>BO<sub>3</sub> is heated to form B<sub>2</sub>O<sub>3</sub> by dehydration, which can react with urea or the decomposed product of urea to form BN. Meanwhile, urea is pyrolyzed into various CN gases (C<sub>2</sub>N<sub>2</sub><sup>+</sup>, C<sub>3</sub>N<sub>2</sub><sup>+</sup>, and C<sub>3</sub>N<sub>3</sub><sup>+</sup>),<sup>32</sup> which reduce Co<sup>2+</sup> to metallic cobalt and serve as a carbon source for the growth of carbon nanotubes (CNTs) *in situ* on the BN surface with the aid of cobalt catalyst. Fig. S1a† shows pictures of the prepared samples with and without cobalt(II) acetate. With cobalt(II) acetate, the synthesis yielded a black powder named as p-BN/CNTs, while the sample prepared without cobalt(II) acetate is a white powder, named as O-BN. Scanning electron microscopy (SEM) image shows that p-BN/CNTs (Fig. S1b†) has a loose and porous structure with carbon nanotubes woven into a 3D conductive network, which ensures a high electrode integrity and fast electron transport. Transmission electron microscopy (TEM) images (Fig. 1a and b) of p-BN/CNTs show that the CNTs with diameters of 10–50 nm are connected with some particles. The distance between two neighboring bright reflections of the particles is 0.258 nm (Fig. 1c), which perfectly correspond with

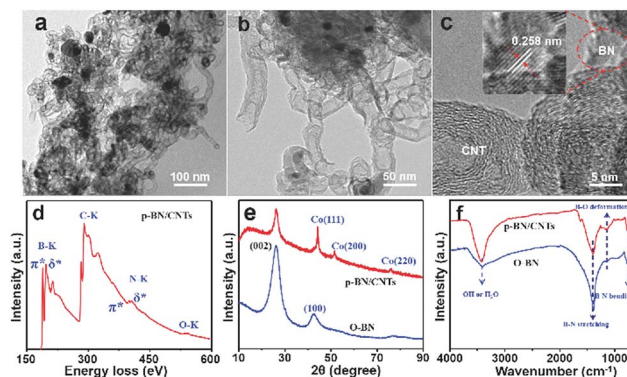


Fig. 1 (a–c) TEM images of p-BN/CNTs. (d) Representative EELS spectrum of p-BN/CNTs. (e) X-ray diffraction patterns of p-BN/CNTs and O-BN. (f) FTIR spectra of p-BN/CNTs and O-BN.

the N–N or B–B atom separations in h-BN (002) planes.<sup>33</sup> Elemental compositions of p-BN/CNTs were investigated using electron energy loss spectroscopy (EELS). Fig. 1d displays the core-loss K-edges of B, C, N and O located at 188, 284, 401 and 532 eV, respectively. The sharply defined 1s  $\rightarrow$   $\pi^*$  and 1s  $\rightarrow$   $\delta^*$  transition features of the B and N K-edges are characteristics of the honeycomb sp<sup>2</sup>-hybridized BN networks.<sup>34</sup> Metallic cobalt produced in the p-BN/CNTs samples (Fig. 1e) is confirmed by the three typical peaks at 44.2°, 51.6°, and 75.9°, consistent with respective (111), (200), and (220) planes of Co (PDF# 89-4307). Because the (002) planes of BN and CNTs overlap, the peak observed at  $2\theta = 26.2^\circ$  could be assigned to the (002) plane of hexagonal boron nitride (JCPDS card no. 34-0421) or CNTs (JCPDS card no. 41-1387) for the p-BN/CNTs sample. No diffraction patterns related to B<sub>2</sub>O<sub>3</sub> were observed. O-BN exhibits two characteristic XRD peaks at 26.1° and 42.8°, which are attributed to (002) and (100) planes, respectively, of the graphitic structure of BN.

Fourier transform infrared (FTIR) spectra of p-BN/CNTs and O-BN (Fig. 1f) both exhibit two characteristic absorption bands at 1380 and 780 cm<sup>-1</sup>, attributed to B–N stretching and B–N bending of BN, respectively, which is consistent with previously reported results.<sup>35</sup> Additionally, a broad peak at 3410 cm<sup>-1</sup> is attributed to the O–H stretching vibrations or water molecules, and is widely observed in the BN systems. The weak peak at 1190 cm<sup>-1</sup> is assigned to B–O deformation originating from the hydroxyl group.<sup>36</sup> Moreover, the intense peak centered at approximately 1344 cm<sup>-1</sup> in Raman spectrum of p-BN/CNTs maybe the superimposition of the D peak of carbon and E<sub>2g</sub> vibration mode of BN (Fig. S2a†).<sup>37</sup> On the basis of TEM, EELS, XRD, FTIR and Raman spectrum results, the sample p-BN/CNTs is concluded to be composed of Co, BN and CNTs. The Co content in the p-BN/CNTs matrix is 7.9 wt% as measured by ICP and the content of BN is 31.2 wt% as determined by thermogravimetric analysis (TGA, Fig. S2b†).

CNTs growth probably undergoes the typical tip growth mode (Fig. S3†), where the metallic cobalt act as a catalyst and BN acts as the substrate.<sup>38</sup> To further confirm this mechanism, control experiment was performed. As shown in Fig. S4a and b,†

only carbon wrapped metallic cobalt were obtained, instead of no CNTs, without using  $\text{H}_3\text{BO}_3$  during the preparation, revealing that BN act as substrate for the growth of CNTs. These results also confirm that the mechanism of p-BN/CNTs formation is reasonable. Importantly, this growth mode can facilitate seamless interconnections between BN and CNTs (Fig. 1c), remarkably lowering the contact resistance and improving electron transport compared to simple physical mixing CNTs with BN. The conductivity of p-BN/CNTs is  $1884 \text{ S m}^{-1}$ , as determined by a 4-point probe measurement, which is an order of magnitude higher than those of carbon blacks, such as Vulcan XC-72 carbon ( $150 \text{ S m}^{-1}$ ).<sup>39</sup>

The chemical composition and the covalent bonding in the p-BN/CNTs sample were further analyzed by X-ray photoelectron spectroscopy (XPS). The relative atomic contents of C, N, B and O in the p-BN/CNTs sample are calculated from the XPS survey spectrum (Fig. S5a†) to be approximately 64.1%, 13.0%, 13.3%, and 9.2%, respectively. The Co signal at  $\sim 775 \text{ eV}$  is negligible because the Co nanoparticles are embedded in BN and wrapped in CNTs. The C 1s spectrum (Fig. 2a) is divided into five peaks at approximately 284.6, 285.8, 287.2, 289.3 and 291.4 eV, corresponding to the typical C-C/C=C of graphitic carbon, C=N, N-C=O, C-O and C-R species, respectively, with C-C/C=C of graphitic carbon being the main component.<sup>40</sup> The high-resolution XPS spectrum of O 1s (Fig. 2b) shows that the element O has been introduced to the carbon and BN material, which improves its LiPSs binding ability. Besides, the N 1s core level can be fitted into four typical peaks at the binding energies of 398.0, 398.5, 399.3 and 400.3 eV (Fig. 2c), consistent with N-B, pyridinic, pyrrolic, and graphitic nitrogens, respectively.<sup>35,41</sup> This confirms that the carbon is doped with N during the pyrolysis process of urea. Among these nitrogen heteroatoms, the pyrrolic-N and pyridinic-N have lone pair electrons and high electronegativity. Thus, they can adsorb positively charged  $\text{Li}^+$  in LiPSs by forming  $\text{LiS}_n\text{Li}^+\cdots\text{N}$  bond, thereby resulting in an effective trapping of LiPSs.<sup>42</sup> Moreover, the recorded B 1s peak

(Fig. 2d) can be fitted with two modes located at 190.8 and 191.8 eV. The former peak derives from the main  $\text{BN}_3$  component.<sup>43</sup> The latter is caused by the presence of oxygen-substituted  $\text{BN}_2\text{O}$  structure, which possesses peaks at binding energies 1–2 eV lower than the characteristic peaks of  $\text{B}_2\text{O}_3$  or boric acid.<sup>44</sup> Moreover, the prepared sample has been intensively washed with hot water to remove  $\text{B}_2\text{O}_3$ . The presence of conjugated  $\text{BN}_2\text{O}$  structure verifies the embedding of O atoms into the BN lattice at the original N positions.<sup>45</sup> It should be noted that the introduction of oxygen into BN can not only improve its electrical conductivity by narrowing the bandgap, but also enhance its binding strength to the LiPSs species.<sup>46</sup> Therefore, p-BN/CNTs matrix can be deduced to effectively trap LiPSs through strong interactions.

The strong interaction between the p-BN/CNTs matrix and  $\text{Li}_2\text{S}_6$  is further confirmed by XPS analysis. As shown in Fig. S5b–d,†  $\text{Li}_2\text{S}_6$  exhibits two sulfur contributions in its S 2p spectrum at 161.5 and 163.8 eV, corresponding to the terminal sulfur ( $\text{S}_\text{T}^{-1}$ ) and bridging sulfur ( $\text{S}_\text{B}^0$ ) atoms, respectively.<sup>47</sup> It is noted that the S–O bond in the prepared  $\text{Li}_2\text{S}_6$  sample might be due to air oxidation of  $\text{Li}_2\text{S}_6$  during the sample transfer for XPS analysis. Compared with  $\text{Li}_2\text{S}_6$ , the  $\text{Li}_2\text{S}_6$  bonded to O-BN exhibits two higher bonding energy contributions in the S 2p spectrum with S  $2p^{3/2}$  at 162.1 and 164.7 eV, representing shifts of 0.6 eV and 0.9 eV for  $\text{S}_\text{T}^{-1}$  and  $\text{S}_\text{B}^0$ , respectively. Similarly, the  $\text{Li}_2\text{S}_6$  bonded to p-BN/CNTs exhibits two higher bonding energy contributions in the S 2p spectrum with S  $2p^{3/2}$  at 162.2 and 164.8 eV, representing shifts of 0.7 and 1.0 eV for  $\text{S}_\text{T}^{-1}$  and  $\text{S}_\text{B}^0$ , respectively. This is due to the polarization of electrons away from the sulfur atoms in O-BN and p-BN/CNTs, suggesting that  $\text{Li}_2\text{S}_6$  can chemically interact with O-BN and p-BN/CNTs.<sup>48</sup>

As mentioned above, the p-BN/CNTs matrix traps LiPSs through chemisorption, thus a high specific surface area associated with abundant chemical sites is essential. Nitrogen adsorption isotherms (Fig. 3a) show that p-BN/CNTs has a high surface area of  $168 \text{ m}^2 \text{ g}^{-1}$  and pore volume of  $0.33 \text{ cm}^3 \text{ g}^{-1}$ , which is higher than most polar metallic compounds listed in Table S1.† We also measured the surface area and pore volume of O-BN, which are  $291 \text{ m}^2 \text{ g}^{-1}$  and  $0.30 \text{ cm}^3 \text{ g}^{-1}$ , respectively. The pore size distributions of O-BN, p-BN/CNTs and O-CNTs are shown in Fig. S6.† The  $\text{Li}_2\text{S}_6$  solutions mixed with O-BN and p-BN/CNTs show more obvious discoloration than that mixed with O-CNTs (Fig. S7†). UV/Vis absorption spectroscopy was used to quantitatively evaluate the adsorptivity of p-BN/CNTs and O-BN toward LiPSs (Fig. S8†).<sup>49</sup> The adsorptivity values of p-BN/CNTs, O-BN and O-CNTs were calculated by the equation (Fig. S8b†) and were illustrated in Fig. 3b. The amounts of  $\text{Li}_2\text{S}_6$  adsorbed by O-BN and p-BN/CNTs are respectively 2.2 and 1.9 times that adsorbed by O-CNTs, strongly indicating that O-doped BN can effectively trap LiPSs in the Li–S battery.

We also demonstrated the merits of p-BN/CNTs as a sulfur host for Li–S battery. The p-BN/CNTs–S composite was prepared via a melt-diffusion method.<sup>50,51</sup> Sulfur existed in a monoclinic phase in the p-BN/CNTs–S composite (Fig. 3c), which is remarkably different from the generally reported orthorhombic phase sulfur. Moreover, sulfur in the S powder, O-BN–S and O-CNTs–S samples existed in a orthorhombic phase (Fig. S9†). The

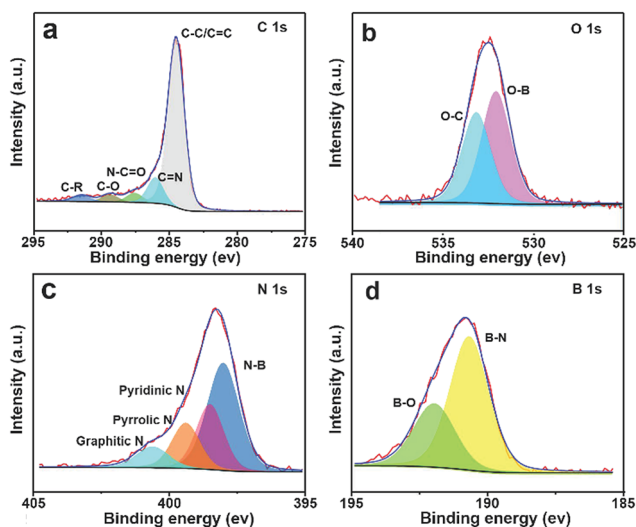


Fig. 2 XPS spectra: (a) C 1s, (b) O 1s, (c) N 1s, and (d) B 1s of p-BN/CNTs.

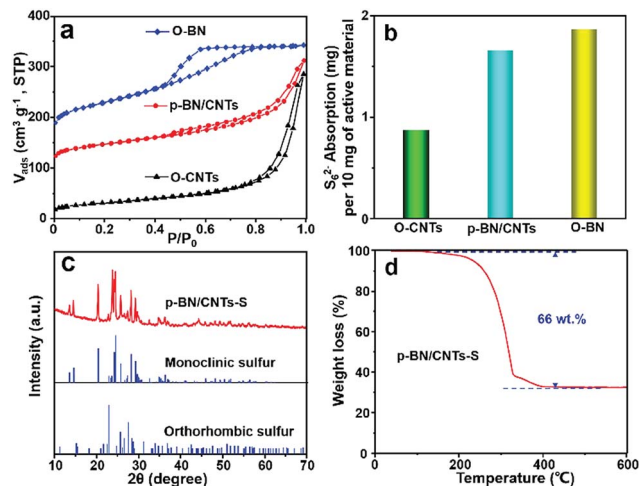


Fig. 3 (a) Nitrogen adsorption isotherms of p-BN/CNTs, O-BN and O-CNTs. The isotherm of p-BN/CNTs is offset vertically by 100 cm<sup>3</sup> g<sup>-1</sup> and O-BN is offset vertically by 150 cm<sup>3</sup> g<sup>-1</sup>, STP. (b) Polysulfide adsorptivity of p-BN/CNTs and O-BN, with comparison to O-CNTs, evaluated by UV/Vis absorption spectroscopy. (c) X-ray diffraction pattern of p-BN/CNTs-S. (d) Thermogravimetric analysis curve of p-BN/CNTs-S.

monoclinic phase favours the high rate performance for lithium-sulfur battery, according to literature,<sup>52</sup> but it exists at temperatures higher than 95.3 °C, whereas the orthorhombic (S<sub>8</sub>), rhombohedral (S<sub>6</sub>) and hexagonal (S<sub>8</sub>) phases are stable at room temperature. We further examined the XRD pattern of p-BN/CNTs-S after storage for two months, and the monoclinic sulfur remained unchanged (Fig. S9†). Such finding strongly indicates that the p-BN/CNTs hybrid has a strong interaction with sulfur, thus ensuring a stable monoclinic phase at room temperature.<sup>53</sup> The sulfur content in the p-BN/CNTs-S composite was 66 wt% as determined by TGA (Fig. 3d). SEM image of the p-BN/CNTs-S composite and the elemental mappings of carbon and sulfur for p-BN/CNTs-S (Fig. S10a-f†) clearly show that sulfur is uniformly distributed in the composite due to the high surface area and large pore volume of p-BN/CNTs.

Cyclic voltammetry (CV) of p-BN/CNTs-S in Fig. 4a revealed a typical electrochemical reaction of reduction and oxidation of sulphur at the cathode. The overlapping cathodic and anodic peaks maintain their sharp shape and display no obvious intensity changes and potential shifts during subsequent cycles.<sup>54</sup> This suggests superior cycling stability and highly reversible redox reactions at the p-BN/CNTs-S cathode. The galvanostatic charge-discharge curves of p-BN/CNTs-S (Fig. 4b) display a typical two-plateau behavior of Li-S battery, and are consistent with the results of CV. Moreover, the flat second discharge plateau at current density as high as 4C indicates a uniform deposition of Li<sub>2</sub>S with small kinetic barriers.<sup>55</sup> The p-BN/CNTs-S cathode yields a reversible discharge capacity of 1374 mA h g<sup>-1</sup> at 0.2C, corresponding to the sulfur utilization of 82.0%. Next, the p-BN/CNTs-S cathode was subjected to cycling at various current densities from 0.2 to 4C for evaluating the rate capability. As shown in Fig. 4c, with increasing current

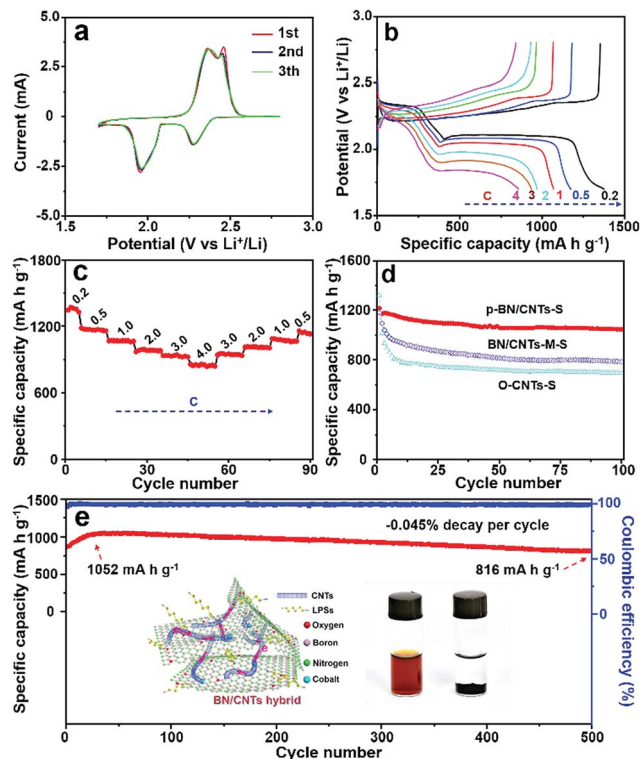


Fig. 4 Electrochemical characterization of p-BN/CNTs-S as the cathode of a Li-S battery. (a) Cyclic voltammetry (CV) measured between 1.7 and 2.8 V at a sweep rate of 0.1 mV s<sup>-1</sup> for the first three cycles. (b) Discharge/charge voltage profiles at various current densities from 0.2 to 4C (1C = 1675 mA g<sup>-1</sup>). (c) Discharge/charge capacity cycled at various current densities from 0.2 to 4C. (d) Capacity retention of material cycled at 0.5C, in comparison with BN/CNTs-M-S and O-CNTs-S materials. (e) Long-term cycling ability and coulombic efficiency of p-BN/CNTs-S at 1C. Specific capacity values were all calculated based on the mass of sulfur.

density, the discharge capacity stabilizes at around 1068, 979, and 840 mA h g<sup>-1</sup> when cycled at 1, 2, and 4C, respectively. When the current density was returned to 0.5C after cycling at different rates, the specific capacity recovered was 1173 mA h g<sup>-1</sup>, indicating very good stability of the p-BN/CNTs-S cathode. The cycling performance of p-BN/CNTs-S cathode at 0.5C (Fig. 4d) shows a relatively good cyclic stability of 1050 mA h g<sup>-1</sup> after 100 cycles. In contrast, the control samples BN/CNTs-M-S (physically mixed BN with CNTs) and O-CNTs-S cathodes show relatively low specific capacities of 787 mA h g<sup>-1</sup> and 695 mA h g<sup>-1</sup>, respectively.

The long-term cycling performance of p-BN/CNTs-S in Fig. 4e shows that, after an activation process, the p-BN/CNTs-S electrode delivers a peak capacity of 1052 mA h g<sup>-1</sup> and retains a high capacity of 816 mA h g<sup>-1</sup> after 500 cycles at 1C, while maintaining a constant coulombic efficiency > 99%. The discharge capacity, rate capability, and cycling stability of p-BN/CNTs-S has rarely been reported in the current studies of Li-S batteries (Tables S2†). High sulfur content and loading are key factors for the commercial applications in Li-S battery. Surprisingly, even though the sulfur content and loading reached 75 wt% and 4.25 mg cm<sup>-2</sup>, respectively, the p-BN/

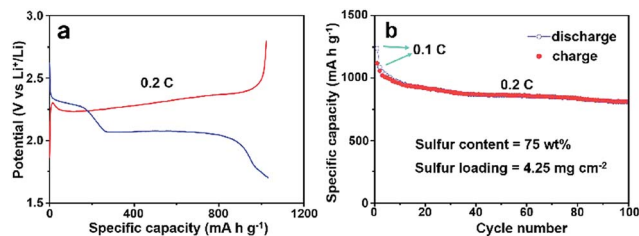


Fig. 5 (a) Discharge/charge voltage profiles at 0.2C, (b) cycling performance of p-BN/CNTs-S with sulfur content of 75 wt% and sulfur loading of 4.25 mg cm<sup>-2</sup>.

CNTs-S electrode (Fig. 5a and b) still exhibits good electrochemical performance with high specific capacity of 1049 mA h g<sup>-1</sup> at 0.2C after activation at 0.1C and remains at 815 mA h g<sup>-1</sup> after 100 cycles.

The extraordinary electrochemical performance of p-BN/CNTs-S cathode can be attributed to the following factors. First, CNTs are tightly connected with BN to form paragenesis structure, which is favorable for rapid electron transfer and electrolyte infiltration, thus improving the utilization of sulfur. Second, oxygen and nitrogen doped carbon nanotubes together with oxygen doped BN can trap polysulfides effectively and thus result in high capacity and stability. At last, the Co nanoparticles in p-BN/CNTs have a positive effect on the capture of sulfur species and lead to significant acceleration of the kinetics of polysulfide redox reactions.<sup>56,57</sup> The paragenesis structure and fast electrode kinetics were supported by the electrochemical impedance spectroscopy (EIS) measurements. A typical Nyquist plot of the composite electrode at various cycling rates (Fig. S11†) reveals a low electrode series resistance (ESR) after activation cycling, which is well maintained after multiple cycles. Moreover, the scanning TEM and the elemental mappings after 50 cycles (Fig. S12†) confirm that sulfur is still uniformly embedded in p-BN/CNT, indicating the structural stability of electrode and the strong interaction of LiPSs with p-BN/CNTs.

## Conclusions

We have developed a one-step co-pyrolysis strategy to fabricate a paragenesis BN/CNTs hybrid as a new high-performance sulfur host for the improvement of rate and cycling performance of Li-S batteries. This hybrid material integrates the advantages of carbon nanotubes, O-doped BN and 3D conductive porous network, exhibiting high electrical conductivity, robust porous framework and effective trapping of polysulfides. Consequently, this material exhibits excellent cycling ability with capacity decay rates as low as 0.045% per cycle, a constant coulombic efficiency of >99% over 500 cycles, and outstanding rate capability up to 840 mA h g<sup>-1</sup> at 4C. Moreover, it exhibits high sulfur-loading areal capacity (up to 4.5 mA h cm<sup>-2</sup>) with a stable cell performance. We believe this work will provide further impetus to explore the fundamental science and applications of BN related nanomaterials in electrochemical energy storage devices.

## Conflicts of interest

There are no conflicts to declare.

## Acknowledgements

This study was supported by the National Science Fund for the National Natural Science Foundation of China (No. 21473021, No. 21776041 and No. 21875028), and Cheung Kong Scholars Programme of China (T2015036).

## Notes and references

- Z. W. She, Y. Sun, Q. Zhang and Y. Cui, *Chem. Soc. Rev.*, 2016, **45**, 5605–5634.
- L. Ma, K. E. Hendrickson, S. Wei and L. A. Archer, *Nano Today*, 2015, **10**, 315–338.
- H.-J. Peng, G. Zhang, X. Chen, Z.-W. Zhang, W.-T. Xu, J. Q. Huang and Q. Zhang, *Angew. Chem., Int. Ed.*, 2016, **55**, 12990–12995.
- R. F. Service, *Science*, 2018, **359**, 1080–1081.
- L. Wang, J. Liu, S. Yuan, Y. Wang and Y. Xia, *Energy Environ. Sci.*, 2016, **9**, 224–231.
- C. Hu, H. Chen, Y. Shen, D. Lu, Y. Zhao, A.-H. Lu, X. Wu, W. Lu and L. Chen, *Nat. Commun.*, 2017, **84**, 79.
- J. Liang, Z.-H. Sun, F. Li and H.-M. Cheng, *Energy Storage Materials*, 2016, **2**, 76–106.
- Y.-X. Yin, S. Xin, Y.-G. Guo and L.-J. Wan, *Angew. Chem., Int. Ed.*, 2013, **52**, 13186–13200.
- T. Wang, K. Kretschmer, S. Choi, H. Pang, H. Xue and G. Wang, *Small Methods*, 2017, **1**, 1700089.
- B. He, W.-C. Li, C. Yang, S.-Q. Wang and A.-H. Lu, *ACS Nano*, 2016, **10**, 1633–1639.
- J. Song, Z. Yu, M. L. Gordin and D. Wang, *Nano Lett.*, 2016, **16**, 864–870.
- Y. Ye, F. Wu, Y. Liu, T. Zhao, J. Qian, Y. Xing, W. Li, J. Huang, L. Li, Q. Huang, X. Bai and R. Chen, *Adv. Mater.*, 2017, **29**, 1700598.
- F. Pei, L. Lin, D. Ou, Z. Zheng, S. Mo, X. Fang and N. Zheng, *Nat. Commun.*, 2017, **8**, 482.
- T. Chen, B. Cheng, G. Zhu, R. Chen, Y. Hu, L. Ma, H. Lv, Y. Wang, J. Liang, Z. Tie, Z. Jin and J. Liu, *Nano Lett.*, 2017, **17**, 437–444.
- Q. Pang, D. Kundu, M. Cuisinier and L. F. Nazar, *Nat. Commun.*, 2014, **5**, 4759.
- Z. Li, J. Zhang and X. W. Lou, *Angew. Chem., Int. Ed.*, 2015, **54**, 12886–12890.
- J. Zhang, Z. Li, Y. Chen, S. Gao and X. W. Lou, *Angew. Chem., Int. Ed.*, 2018, **57**, 10944–10948.
- T. Chen, Z. Zhang, B. Cheng, R. Chen, Y. Hu, L. Ma, G. Zhu, J. Liu and Z. Jin, *J. Am. Chem. Soc.*, 2017, **139**, 12710–12715.
- L. Ma, W. Zhang, L. Wang, Y. Hu, G. Zhu, Y. Wang, R. Chen, T. Chen, Z. Tie, J. Liu and Z. Jin, *ACS Nano*, 2018, **12**, 4868–4876.
- X. Liu, J.-Q. Huang, Q. Zhang and L. Mai, *Adv. Mater.*, 2017, **29**, 1601759.

- 21 H. Yao, G. Zheng, P.-C. Hsu, D. Kong, J. J. Cha, W. Li, Z. W. Seh, M. T. McDowell, K. Yan, Z. Liang, V. K. Narasimhan and Y. Cui, *Nat. Commun.*, 2014, **5**, 3943.
- 22 S. B. Patil, H. J. Kim, H.-K. Lim, S. M. Oh, J. Kim, J. Shin, H. Kim, J. W. Choi and S.-J. Hwang, *ACS Energy Lett.*, 2018, **3**, 412–419.
- 23 D. Xiao, C. Lu, C. Chen and S. Yuan, *Energy Storage Materials*, 2018, **10**, 216.
- 24 X. Wang, G. Li, J. Li, Y. Zhang, A. Wook, A. Yu and Z. Chen, *Energy Environ. Sci.*, 2016, **9**, 2533–2538.
- 25 C. Ye, L. Zhang, C. Guo, D. Li, A. Vasileff, H. Wang and S.-Z. Qiao, *Adv. Funct. Mater.*, 2017, **27**, 1702524.
- 26 T. Chen, L. Ma, B. Cheng, R. Chen, Y. Hu, G. Zhu, Y. Wang, J. Liang, Z. Tie, J. Liu and Z. Jin, *Nano Energy*, 2017, **38**, 239–248.
- 27 S. S. Zhang and D. T. Tran, *J. Mater. Chem. A*, 2016, **4**, 4371–4374.
- 28 J. Zhang, C. You, W. Zhang, J. Wang, S. Guo, R. Yang and Y. Xu, *Electrochim. Acta*, 2017, **250**, 159–166.
- 29 D.-R. Deng, F. Xue, Y.-J. Jia, J.-C. Ye, C.-D. Bai, M.-S. Zheng and Q.-F. Dong, *ACS Nano*, 2017, **11**, 6031–6039.
- 30 J. H. Yun, J.-H. Kim, D. K. Kim and H.-W. Lee, *Nano Lett.*, 2018, **18**, 475–481.
- 31 J.-Y. Hwang, H. M. Kim, S.-K. Lee, J.-H. Lee, A. Abouimrane, M. A. Khaleel, I. Belharouak, A. Manthiram and Y.-K. Sun, *Adv. Energy Mater.*, 2016, **6**, 1501480.
- 32 Z. Lin, G. Waller, Y. Liu, M. Liu and C.-P. Wong, *Adv. Energy Mater.*, 2012, **2**, 884–888.
- 33 X. Wang, C. Zhi, L. Li, H. Zeng, C. Li, M. Mitome, D. Golberg and Y. Bando, *Adv. Mater.*, 2011, **23**, 4072–4076.
- 34 C. Zhao, Z. Xu, H. Wang, J. Wei, W. Wang, X. Bai and E. Wang, *Adv. Funct. Mater.*, 2014, **24**, 5985–5992.
- 35 J. Xiong, L. Yang, Y. Chao, J. Pang, M. Zhang, W. Zhu and H. Li, *ACS Sustainable Chem. Eng.*, 2016, **4**, 4457–4464.
- 36 D. Lee, B. Lee, K. H. Park, H. J. Ryu, S. Jeon and S. H. Hong, *Nano Lett.*, 2015, **15**, 1238–1244.
- 37 L. Qin, J. Yu, S. Kuang, C. Xiao and X. Bai, *Nanoscale*, 2012, **4**, 120–123.
- 38 Y. Yan, J. Miao, Z. Yang, F.-X. Xiao, H. B. Yang, B. Liu and Y. Yang, *Chem. Soc. Rev.*, 2015, **44**, 3295–3346.
- 39 Z. Cui, C. Zu, W. Zhou, A. Manthiram and J. B. Goodenough, *Adv. Mater.*, 2016, **28**, 6926–6931.
- 40 Y. Peng, Y. Zhang, J. Huang, Y. Wang, H. Li, B. J. Hwang and J. Zhao, *Carbon*, 2017, **124**, 23–33.
- 41 J. Wang, S. Cheng, W. Li, L. Jia, Q. Xiao, Y. Hou, Z. Zheng, H. Li, S. Zhang, L. Zhou, M. Liu, H. Lin and Y. Zhang, *Nano Energy*, 2017, **40**, 390–398.
- 42 D. Chen, R. Yang, L. Chen, Y. Zou, B. Ren, L. Li, S. Li, Y. Yan and Y. Xu, *J. Alloys Compd.*, 2018, **746**, 116–124.
- 43 X. Gouin, P. Grange, L. Bois, P. L'Haridon and Y. Laurent, *J. Alloys Compd.*, 1995, **224**, 22–28.
- 44 D. J. Joyner and D. M. Hercules, *J. Chem. Phys.*, 1980, **72**, 1095–1108.
- 45 Q. Weng, D. G. Kvashnin, X. Wang, O. Cretu, Y. Yang, M. Zhou, C. Zhang, D.-M. Tang, P. B. Sorokin, Y. Bando and D. Golberg, *Adv. Mater.*, 2017, **29**, 1700695.
- 46 Y. Zhao, L. Yang, J. Zhao, Q. Cai and P. Jin, *Phys. Chem. Chem. Phys.*, 2017, **19**, 18208–18216.
- 47 F. Zhou, Z. Li, X. Luo, T. Wu, B. Jiang, L.-L. Lu, H.-B. Yao, M. Antonietti and S.-H. Yu, *Nano Lett.*, 2018, **18**, 1035–1043.
- 48 S. Mei, C. J. Jafta, I. Lauermann, Q. Ran, M. Kärger, M. Ballauff and Y. Lu, *Adv. Funct. Mater.*, 2017, **27**, 1701176.
- 49 F. Hippauf, W. Nickel, G.-P. Hao, K. Schwedtmann, L. Giebeler, S. Oswald, L. Borchardt, S. Doerfler, J. J. Weigand and S. Kaskel, *Adv. Mater. Interfaces*, 2016, **3**, 1600508.
- 50 X.-Q. Zhang, B. He, W.-C. Li and A.-H. Lu, *Nano Res.*, 2018, **11**, 1238–1246.
- 51 C. Dai, L. Hua, M.-Q. Wang, Y. Chen, J. Han, J. Jiang, Y. Zhang, B. Shen, Y. Niu, S.-J. Bao and M. Xu, *Energy Storage Materials*, 2017, **8**, 202–208.
- 52 S. C. Jung and Y.-K. Han, *J. Power Sources*, 2016, **325**, 495–500.
- 53 S. Moon, Y. H. Jung, W. K. Jung, D. S. Jung, J. W. Choi and D. K. Kim, *Adv. Mater.*, 2013, **25**, 6547–6553.
- 54 L.-H. Zhang, B. He, W.-C. Li and A.-H. Lu, *Adv. Energy Mater.*, 2017, **7**, 1701518.
- 55 J. Liu, W. Li, L. Duan, X. Li, L. Ji, Z. Geng, K. Huang, L. Lu, L. Zhou, Z. Liu, W. Chen, L. Liu, S. Feng and Y. Zhang, *Nano Lett.*, 2015, **15**, 5137–5142.
- 56 Z. Li, C. Li, X. Ge, J. Ma, Z. Zhang, Q. Li, C. Wang and L. Yin, *Nano Energy*, 2016, **23**, 15–26.
- 57 W. Ren, L. Xu, L. Zhu, X. Wang, X. Ma and D. Wang, *ACS Appl. Mater. Interfaces*, 2018, **10**, 11642–11651.